PHYSICAL REVIEW A **101**, 053415 (2020)

Correlation-enhanced high-order-harmonic-generation spectra of Mn and Mn$^+$

Alexander W. Bray,[1] David Freeman,[1] Faiza Naseem,[1] Valeriy K. Dolmatov,[2] and Anatoli S. Kheifets[1]
[1]*Research School of Physics and Engineering, Australian National University, Canberra, Australian Capital Territory 2601, Australia*
[2]*Department of Physics and Earth Science, University of North Alabama, Florence, Alabama 35632, USA*

(Received 24 February 2020; accepted 17 April 2020; published 8 May 2020)

We examine giant resonant enhancement of high-order harmonics generation (HHG) in the Mn atom and its singly charged Mn$^+$ ion. Our theoretical model combines single active electron tunneling and propagation with correlation-enhanced recombination. Previously, this approach demonstrated its useability for the Xe atom [Phys. Rev. A **100**, 013404 (2019)]. Spin-polarized Hartree-Fock and random-phase approximation with exchange calculations are carried out to evaluate the correlation enhancement factor in Mn and Mn$^+$, which is then compared with other reported calculations and the experiment.

DOI: 10.1103/PhysRevA.101.053415

I. INTRODUCTION

Resonant enhancement of high-order harmonics generation (HHG) in atoms and their ionic species has attracted considerable interest as a pathway toward increasing HHG efficiency. Broad giant resonances are well suited toward this goal. In the Xe atom, an enhancement of an order of magnitude is recorded near the giant resonance around the photon energy of 100 eV [1–3]. This resonance is formed by the coupling of the outer $5p$ and inner $4d$ shells and a strong enhancement of the $Ef \to 4d$ recombination channel via trapping the returning photoelectron in the combined field of the ionic core and the centrifugal potential [4]. Similar HHG enhancement is recorded near giant autoionizing resonances (GAR's) in the $3d$ transitional metal atoms and their ions. Here an electron excitation from the inner $3p^6$ shell to a partially filled $3d^n$, $n < 10$ shell gives rise to a GAR in photoionization and reciprocal photorecombination cross sections of the outer $4s$ shell. Accordingly, a strong enhancement of the HHG spectra has been observed experimentally in the neutral Mn atom [5] and the Mn$^+$, Cr$^+$, and Zn$^+$ ions [6–9]. Systematic reviews of these experiments conducted in laser-ablated plasma plumes are presented in Refs. [10–12].

Theoretical treatment of resonantly enhanced HHG has been proposed by various authors. Strelkov [13] developed the so-called four-step model in which the standard three-step scenario for HHG [14,15] has been extended to a fourth step. Namely, the returning photoelectron is captured into an autoionizing state of the parent ion before it recombines into the ground atomic state. Milosêvić [16] suggested that the recombination process could proceed via a coherent superposition of the ground and quasicontinuum (autoionizing) states. These works were followed by Frolov *et al.* [17], who modified their analytic model of HHG [18] to account for the resonant enhancement. In this analytic model, the three steps of the HHG process are represented by three corresponding multiplicative factors. While the atomic resonance does not affect tunneling and laser driven propagation, it can be factored into the recombination cross section, which is simply taken from the corresponding photoionization experiment.

It is the same approach that has been adopted by Shiner *et al.* [1], who compared their resonantly enhanced HHG spectrun of Xe with the corresponding photoionization cross section in the forward emission direction. In our earlier work on correlation enhanced HHG in Xe [19], we implemented a conceptually similar approach. To describe the tunneling and propagation stages of HHG, we solved numerically a time-dependent Schrödinger equation in full dimensionality (3D TDSE) in the single active electron (SAE) approximation. The intershell $4d/5p$ correlation was accounted for during the recombination stage by introducing a multiplicative correlation enhancement factor (CEF). This factor was calculated as the ratio of the two cross sections, one with and another without an account for the intershell correlation. Because of the quasi-one-dimensional nature of the HHG process, both cross sections were evaluated in the polarization direction as $\sigma_z = \sigma(1+\beta)$ with the use of the angular anisotropy β parameter.

In a very recent study on resonantly enhanced HHG in Mn and Mn$^+$, Wahyutama *et al.* [20] introduced a many-electron configuration expansion to seek a basis-based solution of the TDSE. Their HHG spectra displayed a strong enhancement near the 50-eV mark which could be significantly, by nearly two orders of magnitude, reduced by switching off excitations from the $3p$ shell. This served as an evidence of the resonant enhancement of HHG by the $3p \to 3d$ GAR. However, such a strong enhancement is somewhat surprising. Experiments on Mn [5] and Mn$^+$ [7] could only detect an enhancement not exceeding a factor of 10. A similarly modest enhancement in Mn$^+$was also reported in calculation [17] which employed experimental total photoionization cross sections of the Mn$^+$ ion. The latter approach, however, had some inconsistency. Indeed, it is expected that the HHG processes in Mn and Mn$^+$are driven by recombination to the outer valence $4s$ shell. As such, the photoionization cross section from this shell alone should be used in evaluating the enhancement factor. However, this partial cross section is only a small fraction of the total photoionization cross section which is massively dominated by the inner $3d$ shell.

To address these inconsistencies, we adopt our previously developed model [19] and conduct a systematic investigation of resonantly enhanced HHG in Mn and Mn$^+$. We proceed as follows. First, we construct a localized Hartree-Fock (LHF) potentials for Mn and Mn$^+$, which we then plug into the SAE TDSE. From its solution, we generate the HHG spectra for the atomic and ionic species under conditions close to the experiments for Mn [5] and Mn$^+$ [7,8,13]. The resulting HHG spectra are then enhanced by the CEF calculated using the spin-polarized Hartree-Fock method (SP-HF, no correlation) and the spin-polarized random-phase approximation with exchange (SP-RPAE). The latter includes the intershell correlation among the $3p$, $3d$, and $4s$ electrons whereas the former does not. This enhancement allows us to reproduce the experiment on Mn [5] provided we account for a spin-flip excitation in the $4s$ shell [21]. Analogous calculation on Mn$^+$ demonstrates that the HHG spectrum is dominated by the $3d$ shell and, with introduction of the corresponding CEF, the experiments [7,8] can be well reproduced.

The paper is organized into the following sections. In Sec. II, we describe our methods and techniques, both for stationary photoionization and time-dependent HHG calculations. In Sec. III, we present our numerical results and make a comparison with relevant experiments. We conclude by outlining extension of our methods and results to other atomic, ionic, molecular, and condensed-matter systems.

II. METHODS

A. One-electron TDSE and HHG spectrum

We follow closely our previous work [19]. In brief, we solve a one-electron TDSE for a target atom

$$i\partial\Psi(r,t)/\partial t = [\hat{H}_{\rm atom} + \hat{H}_{\rm int}(t)]\Psi(r,t)\ . \tag{1}$$

The angular part of the Hamiltonian is factored out from this expression and represented by the standard spherical harmonics. The radial part of the stationary atomic Hamiltonian

$$\hat{H}_{\rm atom}(r) = -\frac{1}{2}\frac{d^2}{dr^2} + \frac{l(l+1)}{2r^2} + V(r) \tag{2}$$

contains an effective one-electron potential $V(r)$. The latter is constructed as a localized form of the HF potential (LHF). It is generated as prescribed in Ref. [22] from a known continuous radial orbital $P_{\kappa\ell}(r)$ calculated in a frozen HF core:

$$V_{\rm LHF}(r) = \frac{\kappa^2}{2} - \frac{\ell(\ell+1)}{2r^2} + \frac{P''_{\kappa\ell}(r)}{P_{\kappa\ell}(r)} \equiv \frac{Z^*}{r}\ . \tag{3}$$

The LHF potential should be insensitive to the specific choice of the linear κ and orbital ℓ momenta. The effective charge Z^* takes the following asymptotic values:

$$Z^*(r\to 0) = Z\ \ ,\ \ Z^*(r\to\infty) = \begin{cases} 1 & \text{atom} \\ 2 & \text{ion} \end{cases}. \tag{4}$$

The right-hand side (RHS) of expression (3) contains a term divergent near the nodes of the radial orbital $P_{\kappa\ell}(r) = 0$. Outside these nodes, it is interpolated by a smooth function which is approximated by the following analytic expressions:

$$Z^*(r) = be^{-r} + (Z - Z^*_\infty - b)e^{-ar} + Z^*_\infty. \tag{5}$$

TABLE I. Binding energies (in eV) of the Mn atom and Mn$^+$ ion calculated in the HF and LHF approximation and compared to SP-HF calculation and experimental ionization thresholds.

Target	Shell	LHF	HF	SP-HF		Expt.	
Mn	$4s$	9.20	6.83	6.15↓	7.44↑	7.43[a]	8.60[b]
	$3d$	20.8	15.3	17.44		14.3[c]	
Mn$^+$	$4s$	15.6	14.3		14.8↑	15.6[d]	
	$3d$	22.8	23.3	25.4		26[e]	

[a]Ref. [23] ($^7S_3$); [b]Ref. [23] ($^5S_2$); [c]Ref. [24] (^5D); [d]Ref. [23] ($^6S_{5/2}$); [e]Ref. [25].

Here $a = 5.33$ and $b = 9.47$ for Mn and $a = 4.05$ and $b = 5.83$ for Mn$^+$. For both targets, $Z = 25$. Plugging these potentials into the TDSE (1) gives the binding energies of Mn and Mn$^+$ shown in Table I.

The Hamiltonian $\hat{H}_{\rm int}(t)$ describes atomic interaction with the external field and is written in the velocity gauge

$$\hat{H}_{\rm int}(t) = \boldsymbol{A}(t)\cdot\hat{\boldsymbol{p}}\ \ ,\ \ \boldsymbol{E}(t) = -\frac{\boldsymbol{A}(t)}{dt}\ . \tag{6}$$

The vector potential used to describe the linearly polarized (along the $\hat{z}$ axis) driving laser pulse takes the form

$$\boldsymbol{A}(t) = A_0 f(t)\cos(\omega t + \phi)\hat{\boldsymbol{z}}\ . \tag{7}$$

The envelope function $f(t)$ is a Gaussian corresponding to a full-width-half-maximum of intensity. TDSE (1) is solved numerically by the Muller split-propagator method implemented in the computer code [26].

Once the time-dependent wave function $\Psi(r, ts)$ is propagated to a sufficiently long time, the induced dipole moment in the acceleration forms is evaluated as

$$d_A(t) = \langle\Psi(r,t)\left|\frac{dV(r)}{dz} + E(t)\right|\Psi(r,t)\rangle\ , \tag{8}$$

where z is the displacement along the laser polarization axis. The HHG power spectra are obtained by the Fourier transformation of time-dependent dipole moment. The latter is expressed as

$$P_A(\omega) \propto \left|\int_{-T/2}^{T/2} d_A(t)e^{i\omega t}dt\right|^2\ , \tag{9}$$

for a pulse of total duration T.

B. Intershell correlation

Mn is a half-filled shell atom and its electronic structure is conveniently described by the spin-polarized Hartree-Fock (SP-HF) method [27]. According to the Hund's rule, all the spins in the $3d^5$ shell are aligned, thus providing a natural direction for the spin quantization (the "up" direction denoted as ↑ in the following). Because of the exchange interaction, other fully filled shells $n\ell^{2(2\ell+1)}$ are then split into the two half-filled subshells of the opposite spin orientations, $n\ell^{2\ell+1}\uparrow$ and $n\ell^{2\ell+1}\downarrow$. Their binding energies (see Table I) and wave functions differ from each other and can be found as solutions of the corresponding SP-HF equations [27,28]. The SP-HF configuration of the Mn atom is as follows: [Ar] $3d^5\uparrow$ $4s\uparrow$ $4s\downarrow$ ($^6S_{5/2}$). A removal of a spin-up $4s\uparrow$ or spin-down $4s\downarrow$

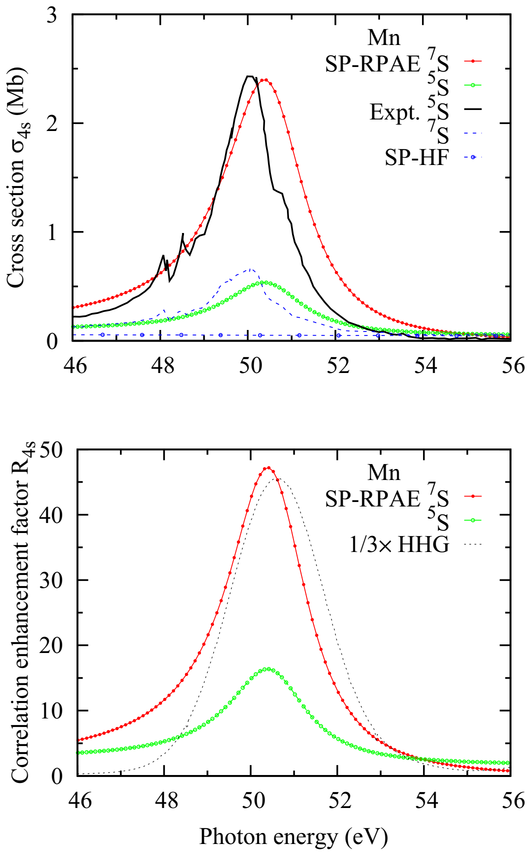

FIG. 1. Top: absolute photoionization cross sections of the $4s$ shell of Mn calculated in the SP-HF and SP-RPAE approximations for various final ionic states. Comparison is made with relative experimental cross sections from Ref. [24], which are internormalized and fitted to the calculated cross section corresponding to the final $^7S_3$ ionic state. Bottom: the correlation enhancement factor $R_{4s} = \sigma_{4s}^{\rm SP-RPAE}/\sigma_{4s}^{\rm SP-HF}$ for the $^7S_3$ and $^5S_2$ ionic states. Also shown is the CEF extracted from the HHG spectra of Ref. [20].

electron from Mn results in two different ion remainders in the ground Mn$^+$ $3d^5\!\uparrow 4s\!\uparrow$ ($^7S_3$) and excited Mn$^+$ $3d^5\!\uparrow 4s\!\downarrow$ ($^5S_2$) states. Multielectron SP-RPAE [28–30] utilizes SP-HF as the zeroth-order independent-particle basis. All the spin-split shells in Mn are fully occupied and the standard formalism of RPAE, developed for closed-shell atoms [31], needs only a minor modification in the SP-RPAE. Namely, the usual RPAE exchange diagrams are discarded for interacting subshells with different spin orientations [29].

III. RESULTS

A. Photoionization cross sections and correlation enhancement factors

Results of the photoionization cross section calculations are shown in Fig. 1 for Mn and Figs. 2 and 3 for Mn$^+$. In the top panel of Fig. 1, we show the absolute photoionization cross sections calculated in the SP-HF and SP-RPAE models. These cross sections correspond to the ion remainder left in the ground $4s^1\!\uparrow$ ($^7S_3$) and the excited $4s^1\!\downarrow$ ($^5S_2$) states. Calculations are compared with relative, but internormalized, experimental cross sections from Ref. [24]. The experimental $^7S_3$ cross section is fitted to the SP-RPAE calculation at its maximum. The bottom panel of Fig. 1 displays the CEF in the form of the photoionization cross-section ratio $R_{4s} = \sigma_{4s}^{\rm SP-RPAE}/\sigma_{4s}^{\rm SP-HF}$ calculated for the $4s\!\uparrow$ and $4s\!\downarrow$ subshells. The calculation [20] allows us to extract a similar factor from their reported HHG spectra. The CEF is constructed as the ratio of the two HHG spectra, one with and another without intershell correlation. The latter spectrum is calculated with the inner $3p$ shell frozen, thus effectively removing the GAR. The HHG generated CEF exhibits sharp oscillations and it is smoothed with a Gaussian convolution (10) with a width parameter $\sigma = 0.5$. A smoothed CEF extracted from the HHG spectra of Ref. [20] is similar in shape to the corresponding SP-RPAE factor for the $^7S_3$ final ionic state, but about three times larger. The same factor for the $^5S_2$ ionic state is smaller by a factor of 4.

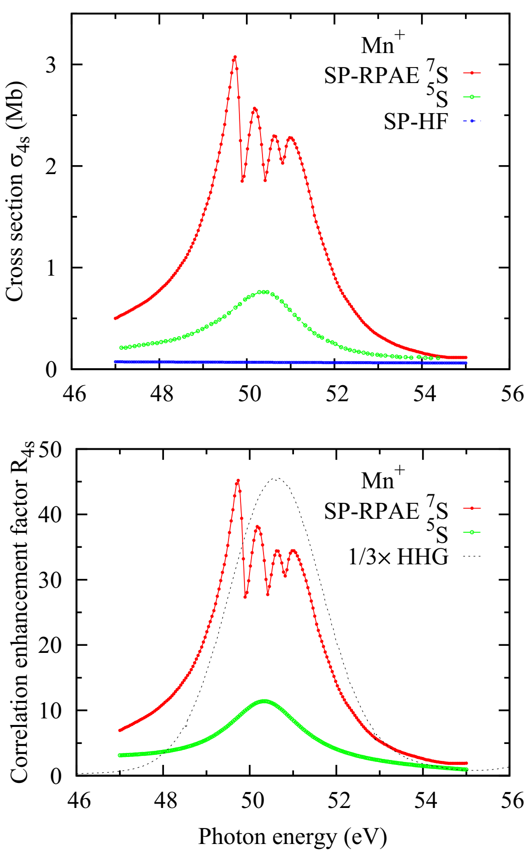

FIG. 2. Same as Fig. 1 but for the Mn$^+$ ion in the $^7S_3$ and $^5S_2$ initial states.

Analogous calculations for the Mn$^+$ ion are exhibited in Figs. 2 and 3. Figure 2 displays the absolute $4s$ photoionization cross sections (top panel) and the CEF $R_{4s} = \sigma_{4s}^{\rm SP-HF}/\sigma_{4s}^{\rm SP-RPAE}$ (bottom panel) for the ground $^7S_3$ and excited $^5S_2$ ionic states. While the magnitude of the $4s$ cross sections is similar between Mn and Mn$^+$, the shape of the cross section and the corresponding enhancement factor is substantially different for the ground $^7S_3$ ionic state. In the latter, the giant $3p\!\downarrow\to 3d\!\downarrow$ resonance overlaps with the spin-orbit split $3p\!\downarrow\to 4s\!\downarrow$ ($^{2,4,6}P$) resonances and the cross section acquires additional resonant peaks [33]. No such structure is visible for the excited $^5S_2$ ionic state in which the $4s\!\downarrow$ state

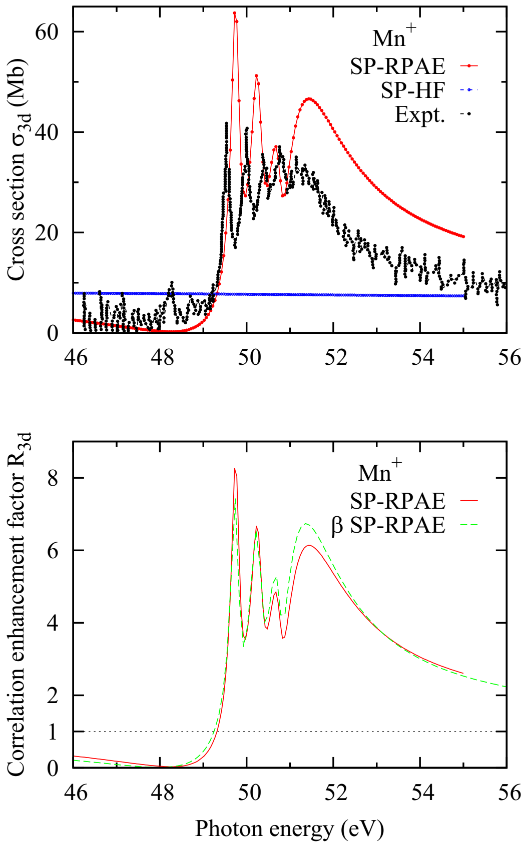

FIG. 3. Same as Fig. 2 but for the $3d$ shell. The top panel displays the total absolute experimental cross section of Mn$^+$ [32]. The bottom panel shows the CEF R_{3d} and the β modified factor in the polarization direction $R_{3d,z}$

is occupied and the transition $3p\downarrow\to 4s\downarrow$ cannot take place. The CEF extracted from the HHG spectra of Ref. [20] does not show the resonant structure of the SP-HF calculation and, when convoluted with a Gaussian, is similar in width with the latter for the $^7S_3$ ionic state.

In Fig. 3, we display the SP-HF and SP-RPAE calculations of the $3d$ partial photoionization cross section of Mn$^+$ in the GAR region. In comparison with the $4s$ cross section displayed in Figs. 1 and 2, the magnitude of the $3d$ cross section is nearly 20 times larger. The total absolute photoionization cross section measured in Ref. [32] generally agrees with the SP-RPAE calculation for the $3d$ shell, but the latter has somewhat larger peak values. The CEF $R_{3d} = \sigma_{3d}^{\rm SP-RPAE}/\sigma_{3d}^{\rm SP-HF}$ is similar in magnitude to that of the $4s$ shell for the Mn$^+$ ion in the excited $^5S_2$ state. Modification of this factor with the β parameter and calculating it in the polarization direction $R_{3d,z} = \sigma_{3d,z}^{\rm SP-RPAE}/\sigma_{3d,z}^{\rm SP-HF}$ has only a marginal effect. It needs to be noted that for energies below the GAR, the CEF $R_{3d} < 1$ and the respective part of the HHG spectrum is suppressed rather than enhanced. This feature of the experimental HHG spectra of the transition ions was emphasized in Ref. [17].

B. HHG spectra

1. *Mn atom*

The HHG spectra of Mn generated from solutions of the SAE TDSE (1) by using Eqs. (8) and (9) are shown in Fig. 4.

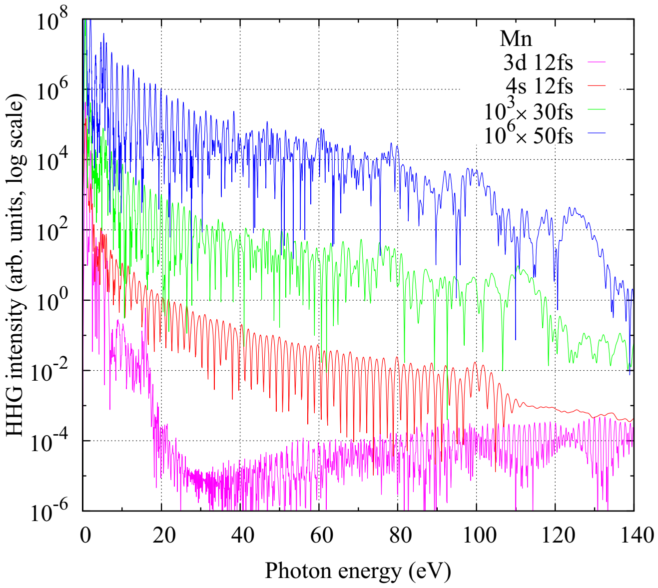

FIG. 4. HHG spectra of Mn generated from SAE TDSE solutions. The driving pulse parameters are as follows: the wavelength $\lambda = 1.8\,\mu$m and the pulse durations (from bottom to top) 12 fs, 30 fs (both at 4×10^{14} W/cm^2), and 50 fs (at 5×10^{14} W/cm^2). The 30- and 50-fs HHG spectra are scaled up for better clarity. All the spectra are calculated for the $4s$ shell except for the 12-fs driving pulse, for which the $3d$ spectrum is also shown without additional scaling.

We simulated the same driving pulse parameters as reported in Ref. [5]. The wavelength was $1.8\,\mu$m and the pulse durations were 12 fs, 30 fs (both at 4×10^{14} W/cm^2), and 50 fs at 5×10^{14} W/cm^2. For the present pulse parameters, the three-step model [14] predicts the HHG cutoff energy $E_c = I_p + 3.17U_p$ above the 400-eV mark, well outside the range of the photon energies shown in the figure. Nevertheless, the 12-fs pulse-driven HHG spectrum does show a visible cutoff at $\approx$100 eV whereas no obviouss cutoff can be identified in other spectra.

All the spectra shown in Fig. 4 are calculated for the $4s$ initial state except for the 12-fs driving pulse. In the latter case, the HHG spectra both for the $4s$ and $3d_{m=0}$ initial states are displayed without any additional scaling. The off-axial magnetic projections $m\neq0$ do not contribute significantly to HHG driven by linearly polarized light. This is so because the electron charge distribution is aligned perpendicular to the driving laser field. Comparison of the $4s$ and $3d_{m=0}$ spectra shows that the former overpasses significantly the later. This is a typical situation when the outer atomic shell is the main contributor to the HHG process. Indeed, tunneling ionization is exponentially suppressed with the binding energy and the ionization potentials of $4s$ and $3d$ differ by a factor of 2 in the Mn atom as shown in Table I.

We notice that the individual harmonics are well resolved in Fig. 4, even for the shortest pulse duration. Indeed, for a transform-limited 12-fs Gaussian pulse at $\lambda = 1.8\,\mu$m, the FWHM is 405 nm or 0.2 eV in equivalence whereas the harmonic spacing $2\omega = 1.3$ eV. However, the individual harmonics are not resolved in the GAR region by Fareed *et al.* [5]. Thus, to make a comparison with the experiment, we apply a

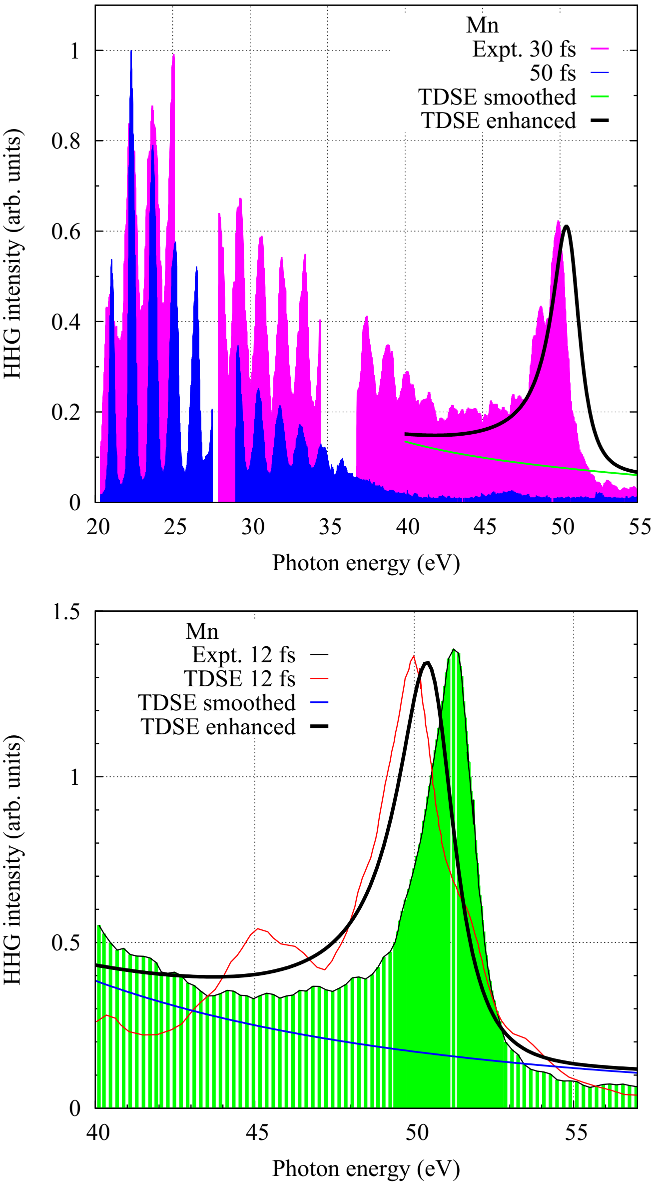

FIG. 5. Top: The experimental HHG spectra [5] recorded with pulse durations of 30 fs (purple spectra) and 50 fs (plum spectra), wavelength of 1.82 μm, and laser intensities of 4×10^{14} W/cm^2 and 5×10^{14} W/cm^2, respectively. The present correlation enhanced TDSE calculation at 30 fs is shown with a solid green line. Bottom: the same set of data for 12-fs pulse duration. Additionally, a TDSE calculation from Ref. [5] is shown.

Gaussian convolution to our raw data:

$$\langle P^{\text{conv.}}(\omega)\rangle = \frac{\int_0^\infty P(\omega')e^{-\sigma(\omega-\omega')^2}d\omega'}{\int_0^\infty e^{-\sigma(\omega-\omega')^2}d\omega'}\,. \tag{10}$$

The raw HHG spectra convoluted with $\sigma = 0.01$ are displayed in Fig. 5 before and after multiplication by the CEF shown on the bottom panel of Fig. 1. These two sets of TDSE calculations are marked as smoothed and enhanced, respectively.

We compare our smoothed and enhanced HHG calculations with the experimental data of Fareed *et al.* [5] corresponding to the 30- and 12-fs driving pulses (the top and bottom panels of Fig. 5, respectively). We notice that the experimental HHG spectra display a distinct cutoff for all driving pulse durations. This cutoff is particularly severe for the longest pulse of 50 fs. One may argue that, because of a low binding energy of only 7.4 eV, the Mn atoms get ionized at the leading edge of the driving pulse under the field intensity that is significantly lower than the peak value. Such a scenario would result in a substantially lower ponderomotive energy and the cutoff.[1] This effect, however, should have been reproduced in our TDSE calculations while in fact it had been missing. So, another explanation should be sought. One can probably identify a medium propagation effect as a culprit which is not accounted for in our single-atom TDSE calculations. In the meantime, our resonantly enhanced HHG spectra agree well with the experiment [5] both at 30 (top panel) and 12 fs (bottom panel). The latter spectrum is also very similar to that calculated from the four-step model of Ref. [13] and reported in Ref. [5].

We note that a good agreement between the experiment [5] and our TDSE calculations is only achieved if we use the CEF corresponding to the ion remainder left in an excited Mn^{+*} state. The CEF for the ionization process leaving Mn$^+$ in the ground state is unreasonably large. The photon absorption alone could not change the spin orientation from $4s\uparrow$ to $4s\downarrow$ electron states. It needs to be a collision-driven excitation that causes such a spin flip. The processes that couple the ground and excited Mn$^+$ ionic states are well documented in dual-laser-plasma experiments [34] and needed to be accounted for in theoretical modeling [21]. It well may be that such ionic excitations are also present in the laser-ablated Mn plasma.

2. *Mn$^+$ ion*

In Fig. 6, we show the HHG spectra of Mn$^+$ ion calculated within our SAE TDSE approach. The top panel displays the calculation at $\lambda = 800$ nm, $I = 8 \times 10^{14}$ W/cm^2, pulse duration 115 fs as in the experiment [8]. In the bottom panel, $\lambda = 400$ nm, $I = 1 \times 10^{15}$ W/cm^2, and the pulse duration is 35 fs as in the experiment [7]. The corresponding HHG cutoffs are shown in the top panel, while on the bottom panel they are outside the displayed photon energy range. The two sets of calculations are visualized starting from the $4s$ and $3d_{m=0}$ bound states. Other $m \neq 0$ components of the $3d$ state make negligible contributions to the HHG spectrum for the reason formulated above. A comparison shown in Fig. 6 indicates that the HHG spectrum generated from the outer $4s$ shell of Mn$^+$ is well below that of the inner $3d$ shell. This is in sharp contrast to the HHG spectra of the neutral Mn atom displayed in Fig. 4. The explanation of such a profound difference may be in the binding energies of the $4s$ and $3d$ states of the neutral and ionized species. While these energies differ by a factor of 2 in the LHF potential for Mn, they are much closer for Mn$^+$.

In Fig. 7, we display the $3d_{m=0}$ HHG spectrum of Fig. 6 enlarged for a narrow photon energy range near the GAR. The top panel displays the raw HHG spectrum and the same spectrum smoothed by Eq. (10) with $\sigma = 5$. We also apply the CEF of Fig. 3 to the smoothed $3d$ spectrum and compare it with the experiment [7]. Both spectra are scaled up for better

---

[1] This argument was brought to us by Vasily Strelkov in his private communication.

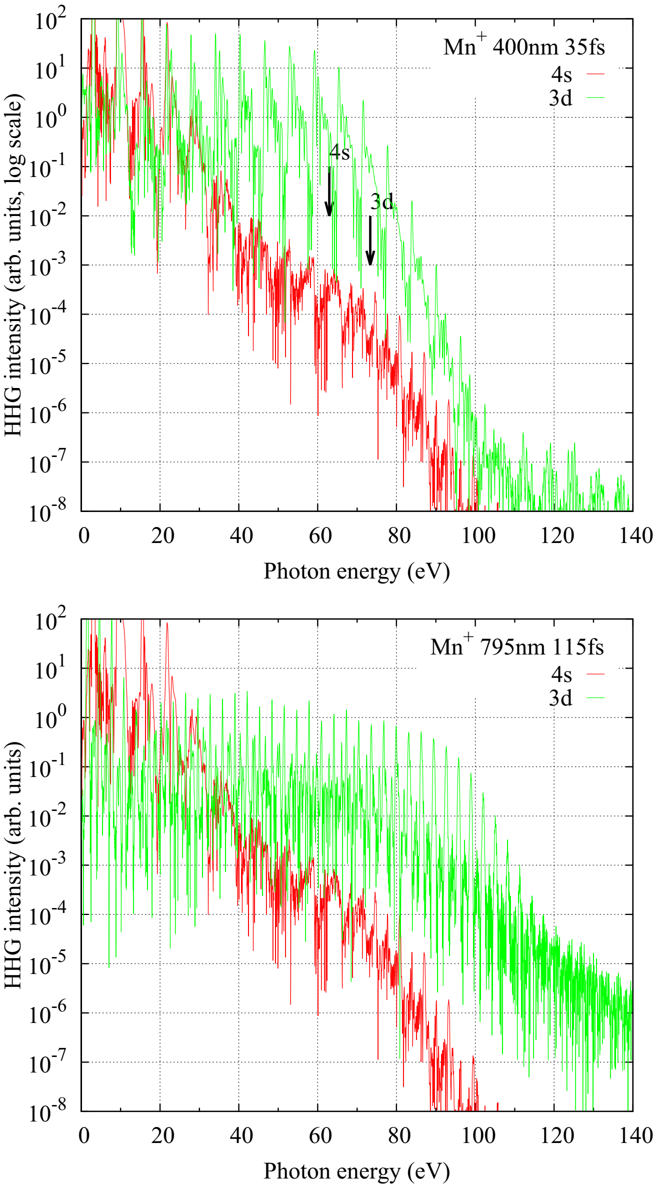

FIG. 6. HHG spectra of Mn$^+$ generated from the 4s and 3$d_{m=0}$ initial states. Top: A 35-fs driving pulse at λ = 400 nm and I =1 × 10^{15} W/cm^2 as in Ref. [7]. The arrows indicate the cutoff energy. Bottom: The driving pulse is 115 fs at λ = 800 nm, I =8 × 10^{14} W/cm^2 as in the experiment [8].

clarity. This comparison is visualized in the bottom panel of Fig. 7 on the linear HHG intensity scale. Our calculation reproduces correctly the resonant harmonic enhancement but suppresses the preceding harmonics somewhat more strongly than in the experiment. Most likely, this difference in the 3d resonantly suppressed region is caused by the HHG contribution of the 4s shell which is normally well below that of 3d.

The same set of data for λ = 400 nm and 35-fs driving pulse is displayed in Fig. 8. Comparison is made with the experiment [7]. Similarly to the case of λ = 795 nm, the enhancement of the resonant harmonics is reproduced correctly while suppression of the preceding harmonic is somewhat stronger than in the experiment. The reason for this extra suppression is formulated in the above paragraph.

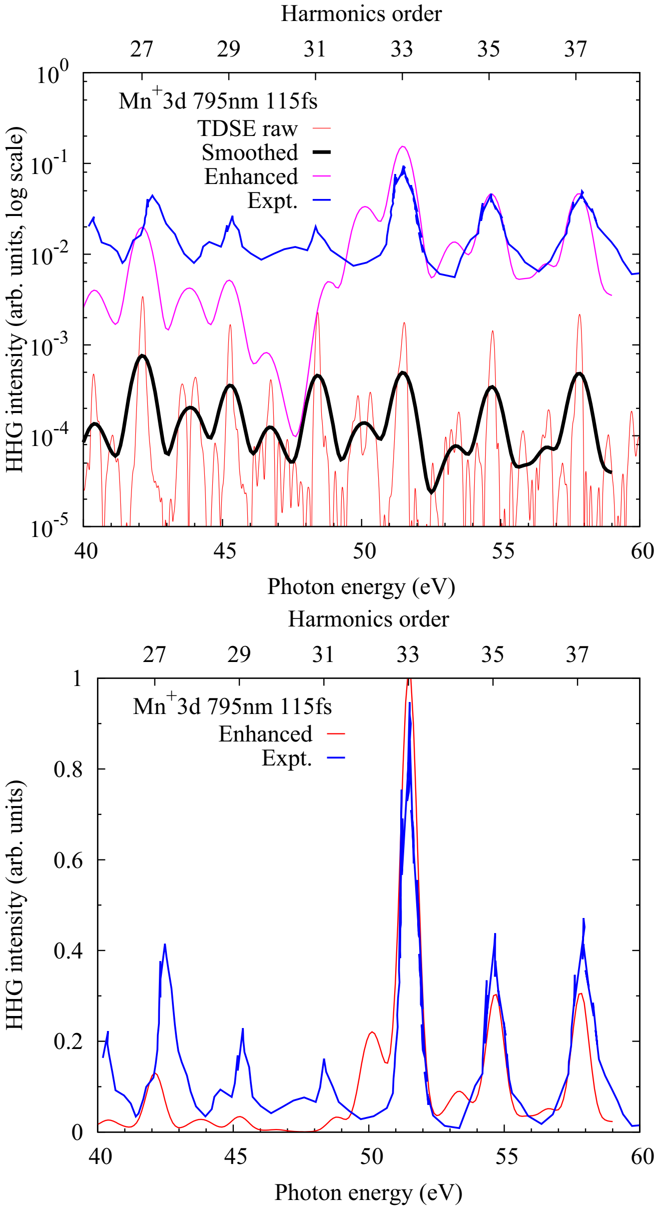

FIG. 7. The 3d HHG spectrum of Fig. 6 is enlarged for the GAR region of Mn$^+$. The top panel displays the raw HHG spectrum, its Gaussian convolution, and multiplicative enhancement with CEF of Fig. 3. The smoothed and enhanced spectra are scaled up for better clarity. Comparison is made with the experiment [8]. In the bottom panel, the enhanced HHG spectrum is compared with the experiment on the linear intensity scale.

IV. CONCLUDING REMARKS

We applied our multiplicative model of resonant enhancement of HHG [19] to the Mn atom and its singly charged ion Mn$^+$ in the region of the giant $3p \rightarrow 3d$ autoionizing resonance. The driving laser pulse parameters are chosen to match those of the recent experiment on Mn [5] and the older measurements in Mn$^+$ [7,8]. Both the 4s and 3$d_{m=0}$ bound states are considered in our single active electron TDSE calculations. While the HHG spectra of Mn are clearly dominated by the tunneling ionization of the 4s initial state, it is the 3d

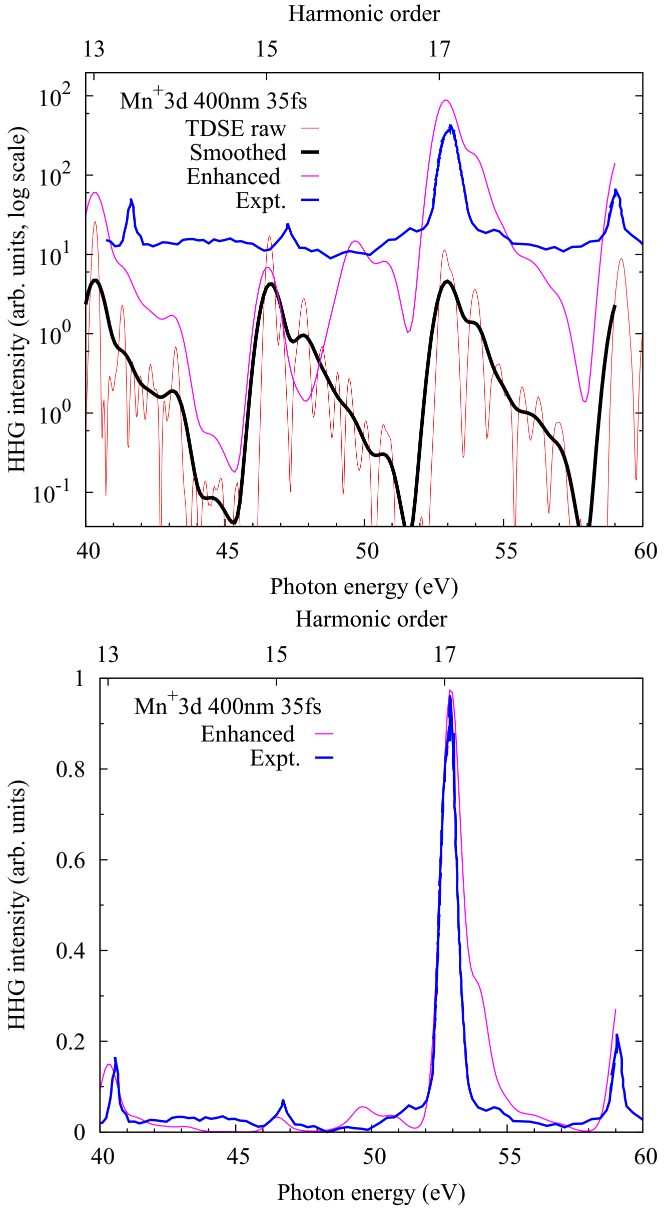

FIG. 8. Same as Fig. 7 for λ = 400 nm and 35-fs driving pulse. Comparison is made with the experiment [7].

bound state that produces much stronger HHG spectra for the Mn$^+$ ion. This difference can be traced back to the ionization potentials of the neutral and ionic species used in our TDSE calculations. When the corresponding multiplicative correlation enhancement factors are applied, the CEF enhanced HHG spectra resemble closely their experimental counterparts. For the neutral Mn atom calculations, we used the CEF evaluated for the outer $4s$ shell whereas the same factor generated for the $3d$ shell was used for the Mn$^+$ ion. While the $4s$ CEF always enhances the HHG spectra, the $3d$ CEF suppresses the harmonics on the low-energy side of the GAR. This behavior was noted in Ref. [17].

The present study serves as a further validation of our multiplicative correlation enhancement model. This model has already been applied to the resonant enhancement of HHG in the Xe atom [19] and found to be in agreement with the experiments [1–3].

Mn is one of several $3d$ transition-metal atoms which display a giant autoionization resonance in their photoionization and photorecombination cross sections. Because this resonance involves the inner shell $3p \to 3d$ transition, it is very resilient to the chemical environment and can be observed in atomic, ionic, molecular, and solid-state targets [34–36]. Several ionic species of $3d$ transition-metal atoms Mn$^+$, Cr$^+$, and Zn$^+$ demonstrate a considerable resonant HHG enhancement in laser-ablated plumes [6–9]. While the present study is focused on Mn$^+$, other ions can be treated in a very similar way. In the future, we intend to include the medium propagation effects by coupling the TDSE with the macroscopic Maxwell equations. Somewhat more challenging, the present technique may be extended to HHG generation in transition metals and their oxides in condensed-matter form.

ACKNOWLEDGMENTS

We thank V. Strelkov for many very stimulating discussions and acknowledge Kenichi Ishikawa for communicating the data of Ref. [20] in a numerical form. The authors are greatly indebted to Serguei Patchkovskii, who placed his iSURF TDSE code at their disposal. Resources of the National Computational Infrastructure (NCI Australia) were employed.

---

[1] A. D. Shiner, B. E. Schmidt, C. Trallero-Herrero, H. J. Worner, S. Patchkovskii, P. B. Corkum, J. C. Kieffer, F. Legare, and D. M. Villeneuve, Probing collective multi-electron dynamics in xenon with high-harmonic spectroscopy, Nat. Phys. **7**, 464 (2011).

[2] D. Faccialà, S. Pabst, B. D. Bruner, A. G. Ciriolo, S. De Silvestri, M. Devetta, M. Negro, H. Soifer, S. Stagira, N. Dudovich *et al.*, Probe of Multielectron Dynamics in Xenon by Caustics in High-Order Harmonic Generation, Phys. Rev. Lett. **117**, 093902 (2016).

[3] D. Faccialà, S. Pabst, B. D. Bruner, A. G. Ciriolo, M. Devetta, M. Negro, P. P. Geetha, A. Pusala, H. Soifer, N. Dudovich *et al.*, High-order harmonic generation spectroscopy by recolliding electron caustics, J. Phys. B **51**, 134002 (2018).

[4] J. P. Connerade, J. E. Esteva, and R. Karnatak (eds.), *Giant Resonance in Atoms, Molecules, and Solids,* Nato Science Series B Vol. 151 (Plenum, New York, 1986).

[5] M. A. Fareed, V. V. Strelkov, M. Singh, N. Thiré, S. Mondal, B. E. Schmidt, F. Légaré, and T. Ozaki, Harmonic Generation from Neutral Manganese Atoms in the Vicinity of the Giant Autoionization Resonance, Phys. Rev. Lett. **121**, 023201 (2018).

[6] R. A. Ganeev, P. A. Naik, H. Singhal, J. A. Chakera, and P. D. Gupta, Strong enhancement and extinction of single harmonic intensity in the mid- and end-plateau regions of the high harmonics generated in weakly excited laser plasmas, Opt. Lett. **32**, 65 (2007).

[7] R. A. Ganeev, L. B. Elouga Bom, J.-C. Kieffer, and T. Ozaki, Systematic investigation of resonance-induced single-harmonic

enhancement in the extreme-ultraviolet range, Phys. Rev. A **75**, 063806 (2007).

[8] R. A. Ganeev, M. Suzuki, M. Baba, and H. Kuroda, High-order harmonic generation from laser plasma produced by pulses of different duration, Phys. Rev. A **76**, 023805 (2007).

[9] R. A. Ganeev, T. Witting, C. Hutchison, F. Frank, M. Tudorovskaya, M. Lein, W. A. Okell, A. Zaïr, J. P. Marangos, and J. W. G. Tisch, Isolated sub-fs XUV pulse generation in Mn plasma ablation, Opt. Express **20**, 25239 (2012).

[10] R. A. Ganeev, Generation of high-order harmonics of high-power lasers in plasmas produced under irradiation of solid target surfaces by a prepulse, Physics-Uspekhi **52**, 55 (2009).

[11] R. Ganeev, *High-Order Harmonic Generation in Laser Plasma Plumes* (Imperial College Press, London, 2012).

[12] R. A. Ganeev, Why plasma harmonics? Quantum Electron. **45**, 785 (2015).

[13] V. Strelkov, Role of Autoionizing State in Resonant High-Order Harmonic Generation and Attosecond Pulse Production, Phys. Rev. Lett. **104**, 123901 (2010).

[14] J. L. Krause, K. J. Schafer, and K. C. Kulander, High-Order Harmonic Generation from Atoms and Ions in the High Intensity Regime, Phys. Rev. Lett. **68**, 3535 (1992).

[15] P. B. Corkum, Plasma Perspective on Strong Field Multiphoton Ionization, Phys. Rev. Lett. **71**, 1994 (1993).

[16] D. B. Miloŝević, Resonant high-order harmonic generation from plasma ablation: Laser intensity dependence of the harmonic intensity and phase, Phys. Rev. A **81**, 023802 (2010).

[17] M. V. Frolov, N. L. Manakov, and A. F. Starace, Potential barrier effects in high-order harmonic generation by transition-metal ions, Phys. Rev. A **82**, 023424 (2010).

[18] M. V. Frolov, N. L. Manakov, T. S. Sarantseva, M. Y. Emelin, M. Y. Ryabikin, and A. F. Starace, Analytic Description of the High-Energy Plateau in Harmonic Generation by Atoms: Can the Harmonic Power Increase with Increasing Laser Wavelengths? Phys. Rev. Lett. **102**, 243901 (2009).

[19] A. W. Bray, D. Freeman, S. Eckart, and A. S. Kheifets, Correlation enhancement of high-order harmonic generation in Xe, Phys. Rev. A **100**, 013404 (2019).

[20] I. S. Wahyutama, T. Sato, and K. L. Ishikawa, Time-dependent multiconfiguration self-consistent-field study on resonantly enhanced high-order harmonic generation from transition-metal elements, Phys. Rev. A **99**, 063420 (2019).

[21] V. K. Dolmatov, On the $3p$ photoabsorption cross section of free Mn^+, J. Phys. B **26**, L79 (1993).

[22] G. Wendin and A. F. Starace, Perturbation theory in a strong-interaction regime with application to $4d$-subshell spectra of Ba and La, J. Phys. B **11**, 4119 (1978).

[23] A. Kramida, Y. Ralchenko, J. Reader, and NIST ASD Team, NIST Atomic Spectra Database, version 5.7.1, National Institute of Standards and Technology, Gaithersburg, MD, https://physics.nist.gov/asd.

[24] M. O. Krause, T. A. Carlson, and A. Fahlman, Photoelectron spectrometry of manganese vapor between 12 and 110 eV, Phys. Rev. A **30**, 1316 (1984).

[25] V. K. Dolmatov and M. Y. Amusia, Resonant structure of the 3d electrons angular distribution in a free Mn^+ ion, J. Phys. B **27**, L281 (1994).

[26] S. Patchkovskii and H. Muller, Simple, accurate, and efficient implementation of 1-electron atomic time-dependent Schrödinger equation in spherical coordinates, Comput. Phys. Commun. **199**, 153 (2016).

[27] J. Slater, *The Self-Consistent Field for Molecules and Solids*, Quantum Theory of Molecules and Solids Vol. 4 (McGraw-Hill, New York, 1974).

[28] M. Y. Amusia and L. V. Chernysheva, *Computation of Atomic Processes: A Handbook for the ATOM Programs* (Institute of Physics, Bristol, UK, 1997).

[29] M. Y. Amus'ya, V. Dolmatov, and V. Ivanov, Photoionization of atoms with half-filled shells, Sov. Phys. JETP **58**, 67 (1983).

[30] M. Y. Amusia and V. K. Dolmatov, Photoionization of inner ns electrons in semifilled shell atoms ($3s$ electrons in a Mn atom), J. Phys. B **26**, 1425 (1993).

[31] M. Y. Amusia, *Atomic Photoeffect* (Plenum Press, New York, 1990).

[32] H. Kjeldsen, F. Folkmann, B. Kristensen, J. B. West, and J. E. Hansen, Absolute cross section for photoionization of Mn^+ in the $3p$ region, J. Phys. B **37**, 1321 (2004).

[33] J. W. Cooper, C. W. Clark, C. L. Cromer, T. B. Lucatorto, B. F. Sonntag, and F. S. Tomkins, Resonant structure in $3p$-subshell absorption of excited and ionized manganese, Phys. Rev. A **35**, 3970 (1987).

[34] J. T. Costello, E. T. Kennedy, B. F. Sonntag, and C. W. Clark, $3p$ photoabsorption of free and bound Cr, Cr^+, Mn, and Mn^+, Phys. Rev. A **43**, 1441 (1991).

[35] B. Sonntag, R. Haensel, and C. Kunz, Optical absorption measurements of the transition metals Ti, V, Cr, Mn, Fe, Co, Ni in the region of $3p$ electron transitions, Solid State Commun. **7**, 597 (1969).

[36] B. Sonntag and P. Zimmermann, XUV spectroscopy of metal atoms, Rep. Progr. Phys. **55**, 911 (1992).